algorithms

MDPI

Article

Parallel Numerical Simulation of 3D Anisotropic Elastic Wave Equations with Sparse Matrix Based on Compact Staggered Finite Difference

Lin Jiang [1,2], Huan Wen [1,2], Ming Wang [1,2], Changjian Zhang [1,2] and Yong Wang [3,*]

[1] Key Laboratory for EOR of Fractured-Vuggy Carbonate Reservoir, SINOPEC, Urumqi 830011, China; jianglin.xbsj@sinopec.com (L.J.); wenh.xbsj@sinopec.com (H.W.); wangming99.xbsj@sinopec.com (M.W.); zhangcj.xbsj@sinopec.com (C.Z.)
[2] Northwest Oilfield Company, SINOPEC, Urumqi 830011, China
[3] Key Laboratory of Exploration Technologies for Oil and Gas Resources, Yangtze University, Ministry of Education, Wuhan 430100, China
* Correspondence: cdwangyong@yangtzeu.edu.cn

Abstract

Numerical simulation of elastic waves in anisotropic media is a fundamental technique for seismic exploration and the characterization of subsurface geological structures. Compared with the conventional finite-difference method, the compact finite-difference method offers higher numerical accuracy and more effective suppression of numerical dispersion, making it well suited for high-precision elastic-wavefield simulations. However, its reliance on derivative-matrix operations imposes significant computational limitations. As the size of the computational domain increases, the derivative matrices grow rapidly in dimension, leading to substantial memory consumption and computational costs, which hinder the efficient simulation of large-scale three-dimensional (3D) anisotropic elastic-wave propagation. To address this limitation, we develop a high-precision discretization scheme for the 3D anisotropic elastic-wave equations based on compact finite-difference theory, while retaining its favorable characteristics of low numerical dispersion and high computational accuracy. To overcome the high memory requirements and low computational efficiency associated with dense derivative matrices, the derivative matrices are sparsified and implemented using sparse matrix storage and operations to eliminate redundant computations. Furthermore, the algorithm is optimized within a parallel computing framework to enable efficient and high-precision numerical simulation of large-scale 3D anisotropic elastic-wave equations. Numerical experiments on representative anisotropic models demonstrate that the proposed sparsified compact finite-difference algorithm preserves the low numerical dispersion and high wavefield accuracy of the conventional compact finite-difference method while substantially reducing memory consumption and computational costs for large-scale models, with significant parallel acceleration. The proposed method accurately and efficiently captures elastic-wave propagation in complex anisotropic media. This study overcomes the limitations of the compact finite-difference method in large-scale numerical simulations and provides an effective computational approach for high-precision, large-scale seismic-wave forward modeling under complex geological conditions.

Keywords: compact staggered finite difference; elastic wave equation; anisotropic medium; 3D numerical simulation; sparse matrix; parallel computing

Check for updates

Academic Editors: Alicia Cordero, Juan Ramón Torregrosa Sánchez and Ramandeep Behl

Received: 10 July 2026
Revised: 23 August 2026
Accepted: 24 August 2026
Published: 27 August 2026

Copyright: © 2026 by the authors. Licensee MDPI, Basel, Switzerland. This article is an open access article distributed under the terms and conditions of the Creative Commons Attribution (CC BY) license.

1. Introduction

Seismic prospecting is an indispensable tool for identifying subsurface resources and characterizing underground geological structures. The propagation of elastic waves is governed by the corresponding wave equations, which provide the fundamental mathematical framework for describing wave propagation in the subsurface. Acoustic and elastic wave equations therefore constitute the theoretical foundation of a wide range of seismic applications, including forward modeling, full-waveform inversion, and subsurface imaging. Accurate numerical solutions of these equations are essential for understanding elastic-wave propagation in heterogeneous geological formations, optimizing seismic data acquisition strategies, and improving the resolution of subsurface structural imaging. Over the past several decades, numerous numerical methods have been developed to solve wave-equation systems, including finite-difference (FD), finite-element (FE), spectral-element (SEM), and integral-equation methods, as well as recently emerging data-driven operator-learning approaches. Among these methods, the finite-difference method remains one of the most widely used approaches in practical applications because of its straightforward implementation and high computational efficiency on structured grids. Etgen and O'Brien sorted out complete technical systems for large-scale three-dimensional acoustic finite-difference forward simulation, which has laid the basic theoretical and technical skeleton for seismic numerical modeling [1]. To boost calculation stability in formations with sharp property variations, Shragge and Tapley constructed a mimetic finite-difference scheme tailored for tensor-form acoustic wave equations [2]. Malovichko and collaborators put forward an acoustic simulation approach built on integral equations, offering a mesh-free numerical solution as another viable option for solving wave propagation problems [3].

Recent advances in wave simulation research have driven the expansion of three-dimensional (3D) wavefield modeling scope, shifting from conventional acoustic media to more complex elastic and anisotropic geological environments. Acoustic wave simulation has long been a research hotspot in geophysical exploration and engineering geophysics, with abundant mature research achievements accumulated. Lecoulant et al. conducted 3D numerical modeling of earthquake-induced acoustic waves in marine environments, which validated the practical applicability of acoustic simulation techniques for environmental geophysical analysis [4]. Vidana Morales and colleagues established a 3D finite element simulation framework targeted at acoustic resonant systems, which delivers high-precision calculation of structural resonant responses [5]. Yang's team further extended the conventional acoustic simulation theory to acoustoelastic media, successfully incorporating pre-stress influence factors into the 3D elastic wave propagation calculation system [6]. In recent years, physics-informed neural operators have emerged as a novel technical approach for wavefield prediction tasks. Zhang et al. adopted Fourier neural operators to solve elastic wave equations, and experimental results verified the excellent generalization performance of this algorithm in various wave simulation scenarios [7].

A variety of numerical methods have also been applied to 3D elastic-wave simulation, including finite difference, spectral element and discontinuous Galerkin methods. To optimize the efficiency of 3D elastic wave numerical calculation, Lehmann et al. proposed a factorized Fourier neural operator (F-FNO) framework. This method greatly improves computational speed while retaining calculation accuracy within a reasonable range [8]. Focusing on complex anisotropic geological structures, He et al. constructed a discontinuous Galerkin algorithm based on tetrahedral meshes for 3D transversely isotropic (TI) media, which effectively enhances the geometric adaptability of numerical simulation for irregular underground structures [9]. Zou's research group developed deep neural Helmholtz operators applicable to 3D elastic wave propagation and inversion, providing an efficient surrogate modeling solution for large-scale seismic computing problems [10]. Nitka and

Rucka adopted the 3D discrete element method to simulate acoustic emission phenomena caused by rock microcrack initiation and expansion, offering valuable references for revealing the micro-generation mechanism of seismic waves [11]. Li et al. integrated Fourier neural operators with feature-enhanced autoencoders, building an intelligent prediction model for elastic wavefield simulation [12]. Lyu et al. put forward a distributional finite difference scheme and conducted quantitative comparison with spectral element methods to confirm its superior performance in scalability and accuracy for large-scale numerical simulations [13]. Han and Xie designed optimized wavefield reconstruction algorithms for elastic reverse time migration, which effectively improve the imaging quality of actual seismic exploration data [14].

Given the widespread occurrence of anisotropic formations in the subsurface, wave propagation in anisotropic media has become an important research topic in seismic numerical simulation. To solve the imaging distortion problem of elastic reverse time migration in anisotropic environments, Zuo et al. developed a dedicated separation algorithm for 3D anisotropic P-waves and S-waves, which significantly enhances the accuracy of subsurface structural imaging [15]. He et al. extended the application scope of discontinuous Galerkin (DG) methods to TI anisotropic media, forming a stable and reliable numerical simulation system for complex anisotropic wave propagation [9]. Li et al. proposed a combined TLM-CFSPML algorithm for 3D transversely isotropic media, which optimizes the processing effect of absorbing boundaries and suppresses boundary reflection artifacts [16]. Yun et al. performed a comparative analysis of staggered-grid discretization strategies for 3D fractured anisotropic media, and optimized the classic Lebedev discretization scheme to further strengthen the numerical stability and calculation precision of wave simulation [17]. These studies consistently demonstrate that anisotropy substantially increases the complexity of 3D wave simulation and consequently imposes more stringent requirements on the accuracy and stability of numerical discretization schemes.

Despite continuous advances in numerical simulation theories and algorithms, large-scale 3D elastic- and anisotropic-wave modeling still faces substantial computational challenges. The discretization of 3D wave equations requires fine computational grids, inevitably resulting in large memory requirements and high computational costs. Conventional finite-difference methods rely on repeated stencil operations over large computational grids, making it challenging to satisfy the efficiency requirements of high-resolution geological models. To alleviate these computational limitations, various acceleration strategies have been developed. Among them, GPU-based parallel computing has become a major approach for accelerating seismic numerical simulations. Zheng et al. realized GPU parallel acceleration of rotated staggered-grid schemes for anisotropic wave equations, achieving remarkable speedup of numerical calculation [18]. Cao's team built a scalable GPU-accelerated spectral element simulation system to support efficient seismic wave modeling [19]. Tan et al. developed a high-order finite difference forward modeling algorithm based on GPU parallel architecture for 3D seismic wavefield simulation [20]. Cai et al. further integrated multi-GPU hardware acceleration and CUDA-aware MPI communication technology to realize ultra-large-scale 3D elastic wave numerical simulation [21]. In addition, machine learning-based algorithms have also been explored as new acceleration tools for wavefield prediction and surrogate modeling in recent years [22].

In the field of high-precision numerical discretization, compact finite-difference (CFD) methods have attracted increasing attention because of their high resolution and low numerical dispersion. Abdi et al. designed high-order compact discretization schemes for general differential equations, verifying their excellent numerical accuracy and stability through systematic tests [23]. Chen et al. proposed a mixed-order compact generalized

finite difference algorithm suitable for seismic wave numerical simulation [24]. Another study by Chen's team optimized the traditional compact finite difference schemes for two-dimensional acoustic wave equations, effectively improving the suppression effect of numerical dispersion [25]. Pan et al. adopted combined compact discretization strategies to optimize the numerical solving process of acoustic wave propagation equations [26]. Zhou et al. applied high-precision compact finite difference schemes to shear-wave reverse time migration, which greatly improves the clarity and accuracy of subsurface imaging results [27]. Nevertheless, the practical application of existing compact finite difference methods is restricted by inherent defects. Most conventional CFD algorithms depend on dense derivative matrix construction, which will cause excessive memory consumption and huge computational overhead in large-scale 3D wave simulation scenarios. With the continuous expansion of model scale, the scale of derivative matrices increases exponentially, making traditional CFD implementations incapable of adapting to high-performance large-scale computing tasks.

To address the memory and computational-efficiency limitations of conventional compact finite-difference methods in 3D anisotropic-wave simulation, this study develops a high-precision and computationally efficient numerical simulation framework based on an improved compact finite-difference formulation. The key innovation of the proposed method is the sparsification of the derivative matrices, combined with sparse-matrix storage and optimized parallel computing strategies. This approach substantially reduces memory requirements and computational complexity while preserving the high accuracy and low numerical dispersion of the original compact finite-difference formulation. Numerical experiments demonstrate that the proposed framework achieves significant computational acceleration and favorable scalability in large-scale 3D anisotropic-wavefield simulations. The proposed method thus provides an efficient computational solution for high-precision seismic forward modeling in complex anisotropic geological media.

2. Methodology

2.1. 3D Anisotropic Elastic Wave Equations

The wave equation is a type of partial differential equation that describes the physical phenomena and processes associated with wave motion. It expresses the general laws governing wave propagation. The initial and boundary conditions of the wave equation specify the constraints on a particular wave propagation process under given circumstances. Together, the wave equation and these boundary conditions constitute a well-posed problem (also referred to as a boundary-value problem), which describes the specific wave behavior under given conditions. To investigate the characteristics of a particular wave propagation process under specific conditions, it is necessary to solve the corresponding wave equation. For different types of media, such as elastic, viscoelastic, isotropic, and anisotropic media, the wave equations governing wave propagation differ accordingly.

2.1.1. Kinetic Balance Differential Equations

In a perfectly elastic medium, the propagation of elastic waves satisfies the following kinetic balance differential equations.

$$\begin{cases} \rho \frac{\partial^2 u}{\partial t^2} = \frac{\partial \sigma_{xx}}{\partial x} + \frac{\partial \sigma_{xy}}{\partial y} + \frac{\partial \sigma_{xz}}{\partial z} + f_x \\ \rho \frac{\partial^2 v}{\partial t^2} = \frac{\partial \sigma_{yx}}{\partial x} + \frac{\partial \sigma_{yy}}{\partial y} + \frac{\partial \sigma_{yz}}{\partial z} + f_y \\ \rho \frac{\partial^2 w}{\partial t^2} = \frac{\partial \sigma_{zx}}{\partial x} + \frac{\partial \sigma_{zy}}{\partial y} + \frac{\partial \sigma_{zz}}{\partial z} + f_z \end{cases}, \quad (1)$$

where x, y, z denote the spatial coordinate variables, and t denotes the time variable, u, v, w denote the components of the particle displacement in the x, y, z directions, respectively, and

they are functions of x, y, z and t, ρ denotes the density, f_x, f_y, f_z denote the components of the external body force acting on the particle in the x, y, z directions, σ_{xx}, σ_{yy}, σ_{zz}, $\sigma_{yz} = \sigma_{zy}$, $\sigma_{zx} = \sigma_{xz}$, $\sigma_{xy} = \sigma_{yx}$ are the stress components, and their constitutive relation with the strain components ε_{xx}, ε_{yy}, ε_{zz}, $\varepsilon_{yz} = \varepsilon_{zy}$, $\varepsilon_{zx} = \varepsilon_{xz}$, $\varepsilon_{xy} = \varepsilon_{yx}$ satisfies the following generalized Hooke's law, also called the equation of state.

$$\begin{bmatrix} \sigma_{xx} \\ \sigma_{yy} \\ \sigma_{zz} \\ \sigma_{yz} \\ \sigma_{xz} \\ \sigma_{xy} \end{bmatrix} = \begin{bmatrix} C_{11} & C_{12} & C_{13} & C_{14} & C_{15} & C_{16} \\ C_{12} & C_{22} & C_{23} & C_{24} & C_{25} & C_{26} \\ C_{13} & C_{23} & C_{33} & C_{34} & C_{35} & C_{36} \\ C_{14} & C_{24} & C_{34} & C_{44} & C_{45} & C_{46} \\ C_{15} & C_{25} & C_{35} & C_{45} & C_{55} & C_{56} \\ C_{16} & C_{26} & C_{36} & C_{46} & C_{56} & C_{66} \end{bmatrix} \begin{bmatrix} \varepsilon_{xx} \\ \varepsilon_{yy} \\ \varepsilon_{zz} \\ \varepsilon_{yz} \\ \varepsilon_{xz} \\ \varepsilon_{xy} \end{bmatrix}, \tag{2}$$

where $C_{ij}(i, j = 1, 2, \ldots, 6)$ are the elastic parameters, which possess the symmetry property, i.e., $C_{ij} = C_{ji}$. The relationship between strain and displacement satisfies the following geometric equations.

$$\begin{cases} \varepsilon_{xx} = \frac{\partial u}{\partial x}, \quad \varepsilon_{yy} = \frac{\partial v}{\partial y}, \quad \varepsilon_{zz} = \frac{\partial w}{\partial z}, \quad \varepsilon_{yz} = \frac{1}{2}\left(\frac{\partial v}{\partial z} + \frac{\partial w}{\partial y}\right) \\ \varepsilon_{xz} = \frac{1}{2}\left(\frac{\partial w}{\partial x} + \frac{\partial u}{\partial z}\right), \quad \varepsilon_{xy} = \frac{1}{2}\left(\frac{\partial u}{\partial y} + \frac{\partial v}{\partial x}\right) \end{cases} \tag{3}$$

Equations (1)–(3) constitute the wave equations in an arbitrary inhomogeneous and arbitrary anisotropic perfectly elastic medium; in general, they have 21 independent elastic parameters. Substituting Equations (2) and (3) into Equation (1) yields the wave equation in anisotropic media with displacement as the variable.

$$\begin{cases} \rho\frac{\partial^2 u}{\partial t^2} = \frac{\partial}{\partial x}\left[C_{11}\frac{\partial u}{\partial x} + C_{12}\frac{\partial v}{\partial y} + C_{13}\frac{\partial w}{\partial z} + \frac{C_{14}}{2}\left(\frac{\partial v}{\partial z} + \frac{\partial w}{\partial y}\right) + \frac{C_{15}}{2}\left(\frac{\partial w}{\partial x} + \frac{\partial u}{\partial z}\right) + \frac{C_{16}}{2}\left(\frac{\partial u}{\partial y} + \frac{\partial v}{\partial x}\right)\right] \\ + \frac{\partial}{\partial y}\left[C_{16}\frac{\partial u}{\partial x} + C_{26}\frac{\partial v}{\partial y} + C_{36}\frac{\partial w}{\partial z} + \frac{C_{46}}{2}\left(\frac{\partial v}{\partial z} + \frac{\partial w}{\partial y}\right) + \frac{C_{56}}{2}\left(\frac{\partial w}{\partial x} + \frac{\partial u}{\partial z}\right) + \frac{C_{66}}{2}\left(\frac{\partial u}{\partial y} + \frac{\partial v}{\partial x}\right)\right] + \\ \frac{\partial}{\partial z}\left[C_{15}\frac{\partial u}{\partial x} + C_{25}\frac{\partial v}{\partial y} + C_{35}\frac{\partial w}{\partial z} + \frac{C_{45}}{2}\left(\frac{\partial v}{\partial z} + \frac{\partial w}{\partial y}\right) + \frac{C_{55}}{2}\left(\frac{\partial w}{\partial x} + \frac{\partial u}{\partial z}\right) + \frac{C_{56}}{2}\left(\frac{\partial u}{\partial y} + \frac{\partial v}{\partial x}\right)\right] \\ \rho\frac{\partial^2 u}{\partial t^2} = \frac{\partial}{\partial x}\left[C_{16}\frac{\partial u}{\partial x} + C_{26}\frac{\partial v}{\partial y} + C_{36}\frac{\partial w}{\partial z} + \frac{C_{46}}{2}\left(\frac{\partial v}{\partial z} + \frac{\partial w}{\partial y}\right) + \frac{C_{56}}{2}\left(\frac{\partial w}{\partial x} + \frac{\partial u}{\partial z}\right) + \frac{C_{66}}{2}\left(\frac{\partial u}{\partial y} + \frac{\partial v}{\partial x}\right)\right] \\ + \frac{\partial}{\partial y}\left[C_{12}\frac{\partial u}{\partial x} + C_{22}\frac{\partial v}{\partial y} + C_{23}\frac{\partial w}{\partial z} + \frac{C_{24}}{2}\left(\frac{\partial v}{\partial z} + \frac{\partial w}{\partial y}\right) + \frac{C_{25}}{2}\left(\frac{\partial w}{\partial x} + \frac{\partial u}{\partial z}\right) + \frac{C_{26}}{2}\left(\frac{\partial u}{\partial y} + \frac{\partial v}{\partial x}\right)\right] + \\ \frac{\partial}{\partial z}\left[C_{14}\frac{\partial u}{\partial x} + C_{24}\frac{\partial v}{\partial y} + C_{34}\frac{\partial w}{\partial z} + \frac{C_{44}}{2}\left(\frac{\partial v}{\partial z} + \frac{\partial w}{\partial y}\right) + \frac{C_{45}}{2}\left(\frac{\partial w}{\partial x} + \frac{\partial u}{\partial z}\right) + \frac{C_{46}}{2}\left(\frac{\partial u}{\partial y} + \frac{\partial v}{\partial x}\right)\right] \\ \rho\frac{\partial^2 w}{\partial t^2} = \frac{\partial}{\partial x}\left[C_{15}\frac{\partial u}{\partial x} + C_{25}\frac{\partial v}{\partial y} + C_{35}\frac{\partial w}{\partial z} + \frac{C_{45}}{2}\left(\frac{\partial v}{\partial z} + \frac{\partial w}{\partial y}\right) + \frac{C_{55}}{2}\left(\frac{\partial w}{\partial x} + \frac{\partial u}{\partial z}\right) + \frac{C_{56}}{2}\left(\frac{\partial u}{\partial y} + \frac{\partial v}{\partial x}\right)\right] \\ + \frac{\partial}{\partial y}\left[C_{14}\frac{\partial u}{\partial x} + C_{24}\frac{\partial v}{\partial y} + C_{34}\frac{\partial w}{\partial z} + \frac{C_{44}}{2}\left(\frac{\partial v}{\partial z} + \frac{\partial w}{\partial y}\right) + \frac{C_{45}}{2}\left(\frac{\partial w}{\partial x} + \frac{\partial u}{\partial z}\right) + \frac{C_{46}}{2}\left(\frac{\partial u}{\partial y} + \frac{\partial v}{\partial x}\right)\right] + \\ \frac{\partial}{\partial z}\left[C_{13}\frac{\partial u}{\partial x} + C_{23}\frac{\partial v}{\partial y} + C_{33}\frac{\partial w}{\partial z} + \frac{C_{34}}{2}\left(\frac{\partial v}{\partial z} + \frac{\partial w}{\partial y}\right) + \frac{C_{35}}{2}\left(\frac{\partial w}{\partial x} + \frac{\partial u}{\partial z}\right) + \frac{C_{36}}{2}\left(\frac{\partial u}{\partial y} + \frac{\partial v}{\partial x}\right)\right] \end{cases} \tag{4}$$

2.1.2. Stress-Velocity Wave Equations for Anisotropic Elastic Waves

The previous section presented the second-order hyperbolic elastic wave equations with displacement as the primary variable in anisotropic media. When the elastic parameters vary with spatial position, the corresponding wave equation—e.g., Equation (4)—involves partial derivatives of the elastic parameters with respect to the spatial coordinates. At points where the elastic parameters are highly heterogeneous or undergo sharp variations, these partial derivatives may fail to exist. To circumvent this issue, it is sometimes desirable to recast the second-order hyperbolic system in displacement into a first-order hyperbolic system in terms of stress and particle velocity, so that the partial derivatives of the elastic parameters with respect to space no longer appear explicitly.

If we denote by $\dot{u}, \dot{v}, \dot{w}$ the first-order time derivatives of the displacement components u, v, w (i.e., the particle velocities), namely $\dot{u} = \partial u/\partial t$, $\dot{v} = \partial v/\partial t$, $\dot{w} = \partial w/\partial t$ then Equation (1) can be rewritten as:

$$\begin{cases} \rho \frac{\partial \dot{u}}{\partial t} = \frac{\partial \sigma_{xx}}{\partial x} + \frac{\partial \sigma_{xy}}{\partial y} + \frac{\partial \sigma_{xz}}{\partial z} + f_x \\ \rho \frac{\partial \dot{v}}{\partial t} = \frac{\partial \sigma_{yx}}{\partial x} + \frac{\partial \sigma_{yy}}{\partial y} + \frac{\partial \sigma_{yz}}{\partial z} + f_y \\ \rho \frac{\partial \dot{w}}{\partial t} = \frac{\partial \sigma_{zx}}{\partial x} + \frac{\partial \sigma_{zy}}{\partial y} + \frac{\partial \sigma_{zz}}{\partial z} + f_z \end{cases} \tag{5}$$

Substituting Equation (3) into Equation (2), and then taking the first-order time derivative, yields the following:

$$\begin{bmatrix} \frac{\partial \sigma_{xx}}{\partial t} \\ \frac{\partial \sigma_{yy}}{\partial t} \\ \frac{\partial \sigma_{zz}}{\partial t} \\ \frac{\partial \sigma_{yz}}{\partial t} \\ \frac{\partial \sigma_{xz}}{\partial t} \\ \frac{\partial \sigma_{xy}}{\partial t} \end{bmatrix} = \begin{bmatrix} C_{11} & C_{12} & C_{13} & C_{14} & C_{15} & C_{16} \\ C_{12} & C_{22} & C_{23} & C_{24} & C_{25} & C_{26} \\ C_{13} & C_{23} & C_{33} & C_{34} & C_{35} & C_{36} \\ C_{14} & C_{24} & C_{34} & C_{44} & C_{45} & C_{46} \\ C_{15} & C_{25} & C_{35} & C_{45} & C_{55} & C_{56} \\ C_{16} & C_{26} & C_{36} & C_{46} & C_{56} & C_{66} \end{bmatrix} \begin{bmatrix} \frac{\partial \dot{u}}{\partial x} \\ \frac{\partial \dot{v}}{\partial y} \\ \frac{\partial \dot{w}}{\partial z} \\ \frac{1}{2}\left(\frac{\partial \dot{v}}{\partial z} + \frac{\partial \dot{w}}{\partial y}\right) \\ \frac{1}{2}\left(\frac{\partial \dot{w}}{\partial x} + \frac{\partial \dot{u}}{\partial z}\right) \\ \frac{1}{2}\left(\frac{\partial \dot{u}}{\partial y} + \frac{\partial \dot{v}}{\partial x}\right) \end{bmatrix} \tag{6}$$

Equations (5) and (6) constitute the stress-velocity wave equations for arbitrarily heterogeneous and arbitrarily anisotropic elastic media.

2.1.3. Tilted Transverse Isotropy Median

Tilted transversely isotropic (TTI) media are an extension of TI media in which the symmetry axis is not aligned with the global coordinate system but is tilted by an arbitrary angle. This type of anisotropy is commonly used to describe complex geological structures such as dipping shale layers and folded sedimentary formations. Compared with TI media, TTI media introduce additional geometric complexity through rotation of the elastic tensor, while the intrinsic anisotropic properties remain unchanged. The TTI medium can be parameterized using nine physical parameters, including v_p (P-wave velocity), v_s (S-wave velocity), ρ (density), and five anisotropic parameters denoted as ε, γ, δ, θ, φ. Based on this parameterization, the elastic stiffness tensor can be constructed accordingly. The following equation represents the stiffness matrix of a vertical transversely isotropic (VTI) medium.

$$\begin{cases} C'_{11} = C'_{22} = (1+2\varepsilon)\rho v_p^2 \\ C'_{33} = \rho v_p^2 \\ C'_{44} = C'_{55} = \rho v_s^2 \\ C'_{66} = (1+2\gamma)\rho v_s^2 \\ C'_{13} = \rho\sqrt{\left[(1+2\delta)v_p^2 - v_s^2\right]\left(v_p^2 - v_s^2\right)} - \rho v_s^2 \\ C'_{12} = C'_{11} - 2C'_{66} \end{cases}, \; C'_{others} = 0 \tag{7}$$

where C' is the stiffness matrix of a VTI medium. The TTI medium can be obtained by introducing a dip angle (θ) to the VTI medium and applying a coordinate rotation transformation (φ).

2.2. Compact Staggered Finite Difference Method

The staggered grid compact finite difference method (CFDM) is a high-precision numerical solution method improved on the basis of Hermite polynomials. To further enhance the numerical discretization accuracy and stability of staggered grid systems, Boersma et al. optimized and extended the classical Hermite difference formula and

constructed high-order compact finite difference discretization schemes suitable for staggered grid layouts, which can efficiently solve the first-order and second-order derivative terms in fluid mechanics and computational mathematics problems. Among them, the high-precision staggered grid compact finite difference scheme for second-order derivative discretization is given as [28]:

$$\begin{aligned} &a\left(P'_{i-1}+P'_{i+1}\right)+P'_i= \\ &\frac{1}{\Delta x}\sum_{n=1}^{N-1} b_n\left\{P\left[x_i+\frac{2n-1}{2}\Delta x\right]-P\left[x_i-\frac{2n-1}{2}\Delta x\right]\right\} \end{aligned} \tag{8}$$

where a and b are difference coefficients, and Δx denotes the grid spacing. It can be observed from the above equation that the second-order derivative at a given node, the derivatives at adjacent nodes, and the corresponding function values establish a definite equality relationship. By utilizing derivative information from neighboring grid points, this method achieves better numerical stability than the traditional finite difference method (FDM). Converting Equation (8) to matrix form gives Equation (9), from which it is evident that the derivative reduces to matrix multiplication.

$$\begin{cases} \frac{\partial P_1}{\partial x} = \frac{1}{\Delta x} P B_1 A^{-1} \\ \frac{\partial P_2}{\partial x} = \frac{1}{\Delta x} P B_2 A^{-1} \end{cases} \tag{9}$$

where $\frac{\partial P_1}{\partial x}$ and $\frac{\partial P_2}{\partial x}$ are the forward and backward difference derivatives, respectively, and the matrices A, B_1, and B_2 are as follows.

$$\begin{aligned} A &= \begin{bmatrix} 1 & a & & & \\ a & 1 & \ddots & & \\ & \ddots & \ddots & \ddots & \\ & & \ddots & 1 & a \\ & & & a & 1 \end{bmatrix}_{m\times m} \\ B_1 &= \begin{bmatrix} -b_1 & \cdots & -b_n & & \\ b_1 & -b_1 & \ddots & \ddots & \\ \vdots & \ddots & \ddots & \ddots & -b_n \\ b_n & \ddots & \ddots & -b_1 & \vdots \\ & b_n & \cdots & b_1 & -b_1 \end{bmatrix}_{m\times m}, B_2 = \begin{bmatrix} b_1 & \cdots & b_n & & \\ -b_1 & b_1 & \ddots & \ddots & \\ \vdots & \ddots & \ddots & \ddots & b_n \\ -b_n & & \ddots & b_1 & \vdots \\ & -b_n & \cdots & -b_1 & b_1 \end{bmatrix}_{m\times m} \end{aligned} \tag{10}$$

where m denotes the number of grid points in a given direction of the model. As can be seen from the above formula, the discrete coefficient matrix takes the form of a tridiagonal Toeplitz matrix. This reveals that the scheme is essentially a grid-based numerical method featuring strong coupling between grid nodes, which greatly complicates the decoupling of discrete variables. The formula below represents the time recursion formula of the wave field.

$$\begin{bmatrix} \sigma_{xx}^1 \\ \sigma_{yy}^1 \\ \sigma_{zz}^1 \\ \sigma_{yz}^1 \\ \sigma_{xz}^1 \\ \sigma_{xy}^1 \end{bmatrix} = \begin{bmatrix} \sigma_{xx}^0 \\ \sigma_{yy}^0 \\ \sigma_{zz}^0 \\ \sigma_{yz}^0 \\ \sigma_{xz}^0 \\ \sigma_{xy}^0 \end{bmatrix} + C_{6\times 6} \cdot \begin{bmatrix} \frac{\partial \dot{u}}{\partial x_1} \\ \frac{\partial \dot{v}}{\partial y_1} \\ \frac{\partial \dot{w}}{\partial z_1} \\ \frac{1}{2}\left(\frac{\partial \dot{v}}{\partial z_2}+\frac{\partial \dot{w}}{\partial y_2}\right) \\ \frac{1}{2}\left(\frac{\partial \dot{w}}{\partial x_2}+\frac{\partial \dot{u}}{\partial z_2}\right) \\ \frac{1}{2}\left(\frac{\partial \dot{u}}{\partial y_2}+\frac{\partial \dot{v}}{\partial x_2}\right) \end{bmatrix}, \tag{11}$$

$$\begin{bmatrix} \dot{u}^1 \\ \dot{v}^1 \\ \dot{w}^1 \end{bmatrix} = \begin{bmatrix} \dot{u}^0 \\ \dot{v}^0 \\ \dot{w}^0 \end{bmatrix} + \begin{bmatrix} \frac{\sigma_{xx}^1}{\partial x_2} & \frac{\sigma_{xy}^1}{\partial y_1} & \frac{\sigma_{xz}^1}{\partial z_1} \\ \frac{\sigma_{xy}^1}{\partial x_1} & \frac{\sigma_{yy}^1}{\partial y_2} & \frac{\sigma_{yz}^1}{\partial z_1} \\ \frac{\sigma_{xz}^1}{\partial x_1} & \frac{\sigma_{yz}^1}{\partial y_1} & \frac{\sigma_{zz}^1}{\partial z_2} \end{bmatrix}. \tag{12}$$

where $\partial x_1, \partial x_2$ denotes the forward-backward difference described in Equation (9). Furthermore, as the computational model expands in scale, the order of the coefficient matrix increases accordingly. This not only degrades the efficiency of numerical differentiation in simulations but also causes a sharp rise in computational overhead when tackling large-scale problems. Hence, targeted optimizations for this method are urgently needed.

2.3. Sparse Matrix-Based Acceleration

Consider the tridiagonal Toeplitz matrix

$$A_1 = \begin{bmatrix} b_1 & c_1 & 0 & \cdots & 0 \\ a_1 & b_1 & \ddots & \ddots & \vdots \\ 0 & \ddots & \ddots & \ddots & 0 \\ \vdots & \ddots & \ddots & b_1 & c_1 \\ 0 & \cdots & 0 & a_1 & b_1 \end{bmatrix}, \tag{13}$$

where $a_1, c_1 \neq 0$ and b_1 is a constant diagonal coefficient. Such matrices commonly arise from finite difference discretizations of differential operators with nearest-neighbor coupling.

For the above constant-coefficient tridiagonal Toeplitz matrix A_1, its eigenvalues admit analytical expressions [29].

$$\lambda_k = b_1 + 2\sqrt{a_1 c_1}\cos\left(\frac{k\pi}{n+1}\right), k = 1, 2, \ldots, n. \tag{14}$$

Assuming A_1 is nonsingular, its inverse can be written as

$$A_1^{-1} = V\Lambda^{-1}V^{-1}, \tag{15}$$

which implies element-wise representation

$$\left(A_1^{-1}\right)_{ij} = \sum_{k=1}^{n} \frac{1}{\lambda_k} v_{ik} v_{jk}, \tag{16}$$

To further characterize the spatial structure of A_1^{-1}, we consider the associated Green's function formulation. The entries of A_1^{-1} satisfy the recurrence relation

$$a_1 u_{i-1} + b_1 u_i + c_1 u_{i+1} = \delta_{ij}, \tag{17}$$

whose solution leads to a closed-form expression of the form

$$\left(A_1^{-1}\right)_{ij} = C \cdot r^{|i-j|} + O\left(r^{i+j}\right), \tag{18}$$

where r is determined by the characteristic equation

$$c_1 r^2 - b_1 r + a_1 = 0 \tag{19}$$

Let r_1, r_2 be its roots. Under stable and well-conditioned conditions (e.g., strict diagonal dominance or ellipticity of the underlying operator), one root satisfies $|r| < 1$, leading to the dominant asymptotic behavior

$$\left|\left(A_1^{-1}\right)_{ij}\right| \leq C\rho^{|i-j|}, 0 < \rho < 1. \tag{20}$$

This shows that although A_1^{-1} is generally a dense matrix, its entries decay exponentially away from the main diagonal. In particular,

$$\lim_{|i-j|\to\infty}\left(A_1^{-1}\right)_{ij} = 0. \tag{21}$$

Therefore, the inverse matrix exhibits a strong near-diagonal dominance structure despite being fully populated in a strict algebraic sense.

This property reflects the locality of the original discretized operator: A_1 represents nearest-neighbor interactions, while A_1^{-1} describes global influence with exponentially decaying strength over distance. As a consequence, explicitly forming A_1^{-1} is both unnecessary and computationally inefficient. Instead, the linear system $A_1 x = b_1$ is typically solved directly using banded solvers (e.g., Thomas algorithm or banded LU decomposition), preserving computational efficiency and avoiding the $O(n^2)$ storage cost associated with dense inverse matrices.

Based on the above property, although the inverse matrix is theoretically dense, its entries exhibit a strong decay away from the main diagonal. In practical computations, contributions from entries far from the diagonal are several orders of magnitude smaller than those near the diagonal and thus have negligible impact on the numerical solution within machine precision.

Therefore, it is reasonable to retain only the dominant (high-magnitude) entries within a prescribed bandwidth or threshold, while discarding entries below a given tolerance. This leads to a sparse approximation of the inverse-related operator, i.e.,

$$\begin{aligned} &A_1^{-1} \approx \widetilde{A}_1^{-1} \\ &\left(\widetilde{A}_1^{-1}\right)_{ij} = 0 \quad if \quad \left(A_1^{-1}\right)_{ij} < \varepsilon. \end{aligned} \tag{22}$$

Alternatively, a band-limited representation can be introduced as

$$\begin{aligned} &\left(\widetilde{A}_1^{-1}\right)_{ij} = \begin{cases} \left(A_1^{-1}\right)_{ij}, & |i-j| \leq p, \\ 0, & |i-j| > p, \end{cases} \\ &p = 3N \end{aligned} \tag{23}$$

where p denotes the retained bandwidth, N denotes the order of accuracy. Such a sparse representation significantly reduces both memory consumption and computational cost, since only a small fraction of matrix entries are involved in matrix-vector or matrix-matrix operations. Consequently, the overall computational complexity can be reduced while preserving sufficient accuracy for the numerical solution. This sparse structure is particularly suitable for GPU implementation, where memory bandwidth and storage efficiency are critical factors affecting performance. In the present study, a bandwidth with three-fold the order range is adopted.

3. Numerical Examples

To verify the effectiveness of the proposed sparse-matrix acceleration strategy for the compact finite difference method, as well as to ensure that the introduced sparsification

induces negligible accuracy loss, a series of numerical experiments are conducted. The tests are performed on four representative geological models, including homogeneous isotropic media, homogeneous anisotropic media, heterogeneous isotropic media, and heterogeneous anisotropic media, respectively, to comprehensively evaluate the robustness and applicability of the proposed approach.

For each case, the numerical residuals between wavefields obtained with the original compact finite difference scheme and those computed using the sparse-matrix formulation are quantitatively analyzed to assess accuracy preservation. In addition, computational performance is evaluated by comparing the runtime across different model sizes, enabling a systematic investigation of the speedup achieved by the proposed method as the problem scale increases. Table 1 below lists the parameters of homogeneous isotropic and homogeneous anisotropic models, as well as the anisotropy parameters of heterogeneous isotropic and heterogeneous anisotropic models. Figure 1 shows the P-wave fields for heterogeneous isotropic and heterogeneous anisotropic models, where S-wave velocity and density are linearly related to P-wave velocity.

Table 1. Parameters for Four Types of Models.

Model	*Vp* (m/s)	*Vs* (m/s)	Rou (kg/m^3)	ε	γ	δ	θ	φ
homogeneous isotropic	3000	2000	2500	0	0	0	0	0
homogeneous anisotropic	3000	2000	2500	0.35	−0.28	−0.045	45°	60°
heterogeneous isotropic	——	——	——	0	0	0	0	0
heterogeneous anisotropic	——	——	——	0.35	−0.28	−0.045	45°	60°

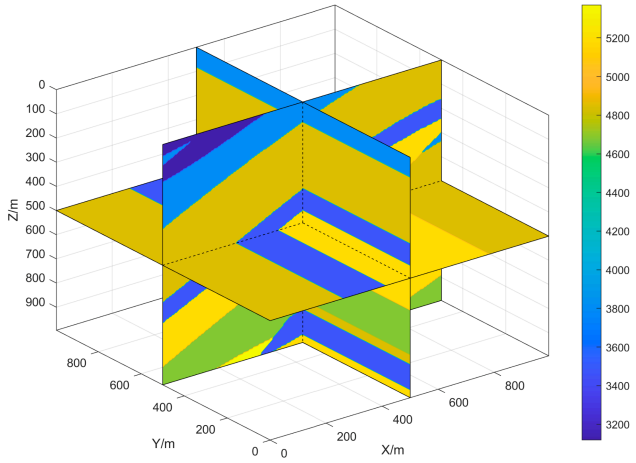


Figure 1. P-Wave velocity distributions of heterogeneous models.

3.1. Numerical Accuracy Comparison

This study conducted forward modeling using four different models. The grid size for all models was 201 × 201 × 201, with 350 time-steps. The spatial sampling interval was 5 m, and the temporal sampling interval was 0.0005 s. A 30 Hz Ricker wavelet was used as the source in the form of point loading and positioned at the center of the model. Meanwhile, a perfectly matched layer (PML) boundary condition with 20 layers was adopted in the numerical simulation to eliminate boundary reflection artifacts. Notably, the sparsification of the finite difference operator only modifies partial matrix coefficients during numerical iteration, which occupies an extremely small proportion of the overall computational resources. Accordingly, the sparsification strategy exhibits a negligible effect on the memory consumption of the three-dimensional numerical simulation.

A comparison was then made between the u wavefield components before and after sparsification of the forward modeling method. Figure 2 below shows a comparison of the u component wavefields in a three-dimensional homogeneous isotropic model.

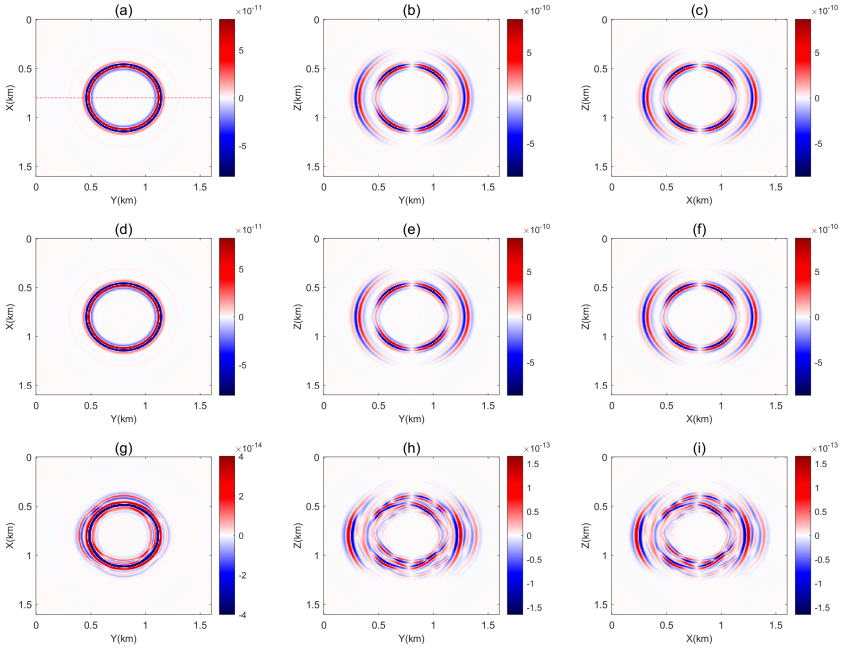


Figure 2. Orthogonal slices of 3D wavefields of the homogeneous isotropic model: (**a**–**c**) wavefields before sparsification; (**d**–**f**) wavefields after sparsification; (**g**–**i**) residual slices between wavefields before and after sparsification. The red dashed line in (**a**) indicates the slice position shown in Figure 3.

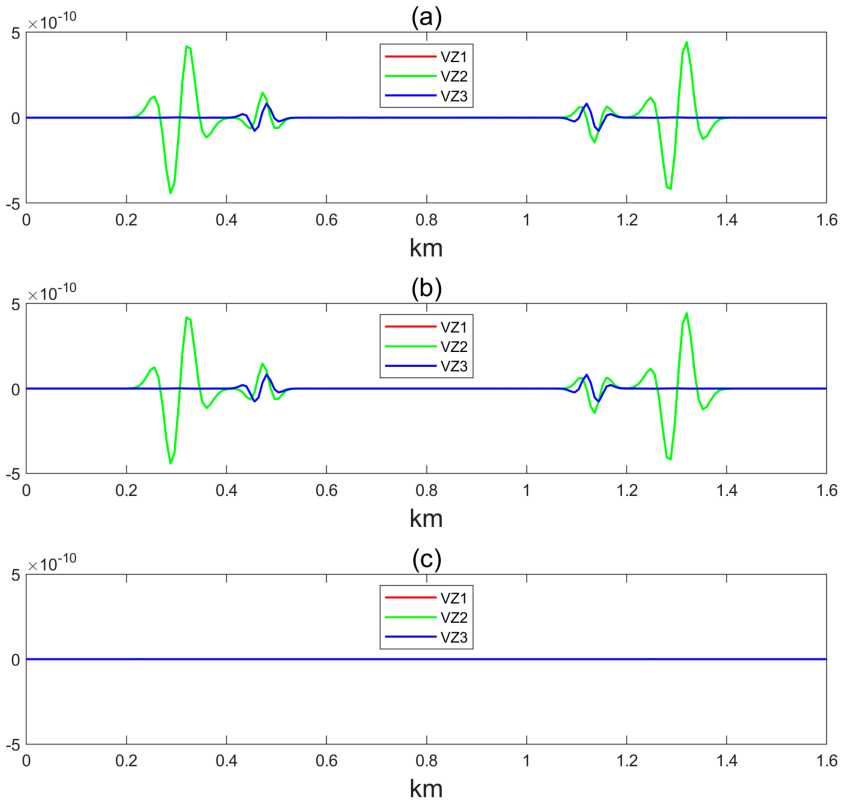


Figure 3. 1D wavefield curves of the homogeneous isotropic model: (**a**) wavefields before sparsification; (**b**) wavefields after sparsification; (**c**) residual curves between (**a**) and (**b**).

Figure 2 displays orthogonal slices of the three-dimensional wavefield for the homogeneous isotropic model, consisting of nine subgraphs arranged in three rows and three columns. Subplots (a)–(c) present orthogonal slices of the original 3D wavefield obtained without sparsification treatment. Subplots (d)–(f) illustrate the corresponding orthogonal wavefield slices after the sparsification strategy is implemented. Subplots (g)–(i) show the residual slices calculated by subtracting the sparsified wavefield from the original wavefield, which quantitatively reflect the difference between wavefield results before and after sparsification.

As illustrated in Figure 2, the wavefield residuals are extremely small, with magnitudes 3–4 orders of magnitude lower than the original wavefield. This indicates that the sparsification algorithm barely affects the forward modeling accuracy for the homogeneous isotropic model. Figure 3 presents the one-dimensional wavefield profiles extracted along the slices shown in Figure 2. It can be further observed from Figure 3 that the two sets of wavefield data are highly consistent, and the relative error calculated from the residuals is only 0.023%.

A comparison was then made between the u wavefield components before and after sparsification of the forward modeling method. Figure 4 below shows a comparison of the u component wavefields in a three-dimensional homogeneous anisotropic model.

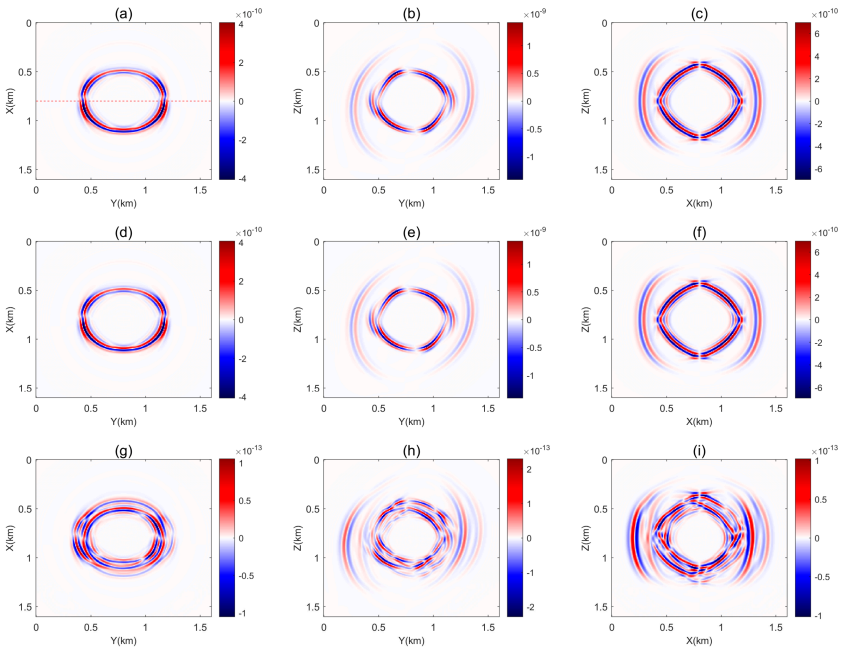


Figure 4. Orthogonal slices of 3D wavefields of the homogeneous anisotropic model: (**a**–**c**) wavefields before sparsification; (**d**–**f**) wavefields after sparsification; (**g**–**i**) residual slices between wavefields before and after sparsification. The red dashed line in (**a**) indicates the slice position shown in Figure 5.

Figure 4 displays orthogonal slices of the three-dimensional wavefield for the homogeneous isotropic model, consisting of nine subgraphs arranged in three rows and three columns. Subplots (a)–(c) present orthogonal slices of the original 3D wavefield obtained without sparsification treatment. Subplots (d)–(f) illustrate the corresponding orthogonal wavefield slices after the sparsification strategy is implemented. Subplots (g)–(i) show the residual slices calculated by subtracting the sparsified wavefield from the original wavefield, which quantitatively reflect the difference between wavefield results before and after sparsification.

As illustrated in Figure 4, the wavefield residuals are extremely small, with magnitudes 3–4 orders of magnitude lower than the original wavefield. This indicates that the

sparsification algorithm barely affects the forward modeling accuracy for the homogeneous isotropic model. Figure 5 presents the one-dimensional wavefield profiles extracted along the slices shown in Figure 4. It can be further observed from Figure 5 that the two sets of wavefield data are highly consistent, and the relative error calculated from the residuals is only 0.03%.

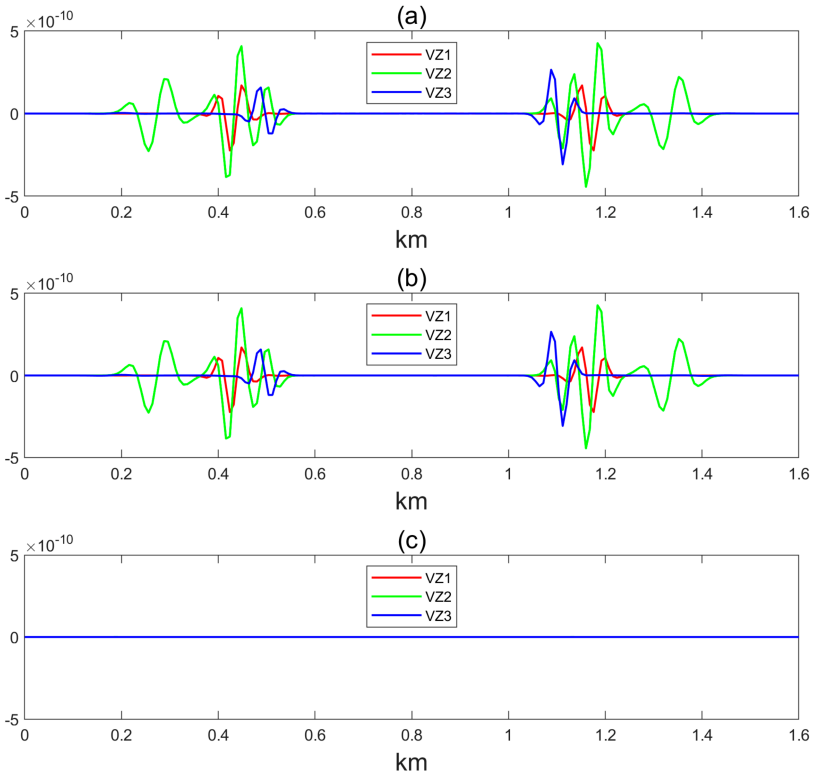


Figure 5. 1D wavefield curves of the homogeneous anisotropic model: (**a**) wavefields before sparsification; (**b**) wavefields after sparsification; (**c**) residual curves between (**a**) and (**b**).

A comparison was then made between the u wavefield components before and after sparsification of the forward modeling method. Figure 6 below shows a comparison of the u component wavefields in a three-dimensional heterogeneous isotropic model.

Figure 6 displays orthogonal slices of the three-dimensional wavefield for the heterogeneous isotropic model, consisting of nine subgraphs arranged in three rows and three columns. Subplots (a)–(c) present orthogonal slices of the original 3D wavefield obtained without sparsification treatment. Subplots (d)–(f) illustrate the corresponding orthogonal wavefield slices after the sparsification strategy is implemented. Subplots (g)–(i) show the residual slices calculated by subtracting the sparsified wavefield from the original wavefield, which quantitatively reflect the difference between wavefield results before and after sparsification.

As illustrated in Figure 6, the wavefield residuals are extremely small, with magnitudes 3–4 orders of magnitude lower than the original wavefield. This indicates that the sparsification algorithm barely affects the forward modeling accuracy for the homogeneous isotropic model. Figure 7 presents the one-dimensional wavefield profiles extracted along the slices shown in Figure 6. It can be further observed from Figure 7 that the two sets of wavefield data are highly consistent, and the relative error calculated from the residuals is only 0.021%.

A comparison was then made between the u wavefield components before and after sparsification of the forward modeling method. Figure 8 below shows a comparison of the u component wavefields in a three-dimensional heterogeneous anisotropic model.

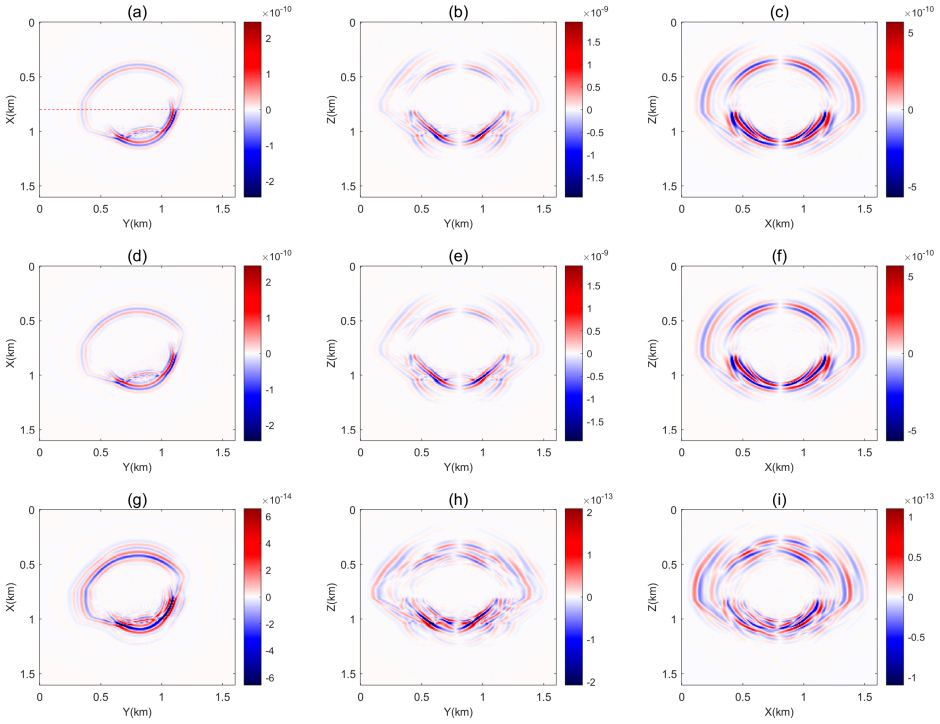


Figure 6. Orthogonal slices of 3D wavefields of the heterogeneous isotropic model: (**a**–**c**) wavefields before sparsification; (**d**–**f**) wavefields after sparsification; (**g**–**i**) residual slices between wavefields before and after sparsification. The red dashed line in (**a**) indicates the slice position shown in Figure 7.

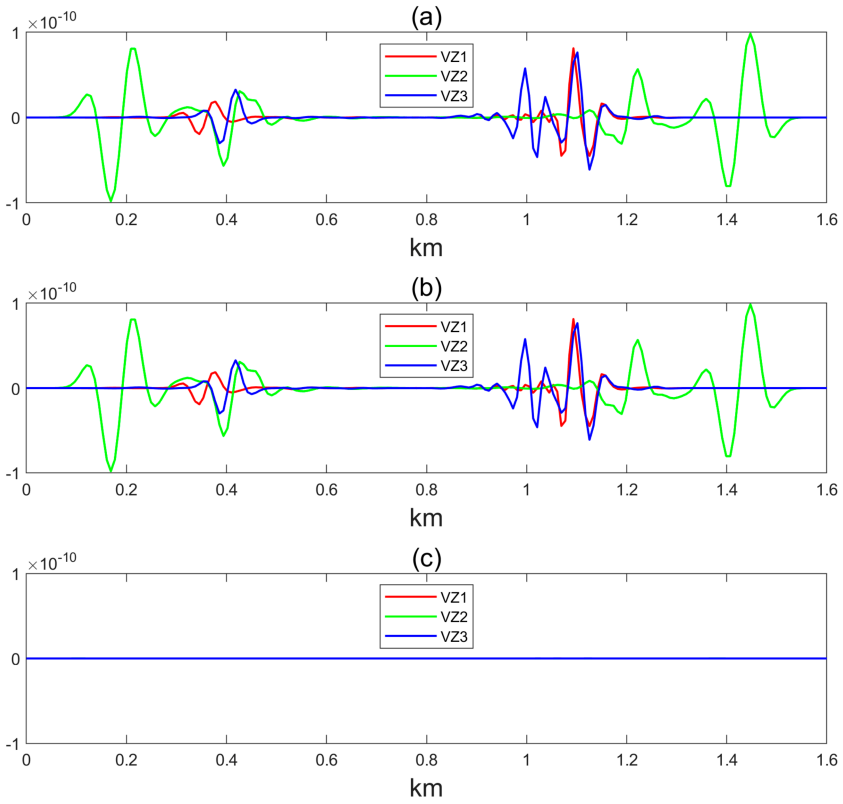


Figure 7. 1D wavefield curves of the heterogeneous isotropic model: (**a**) wavefields before sparsification; (**b**) wavefields after sparsification; (**c**) residual curves between (**a**) and (**b**).

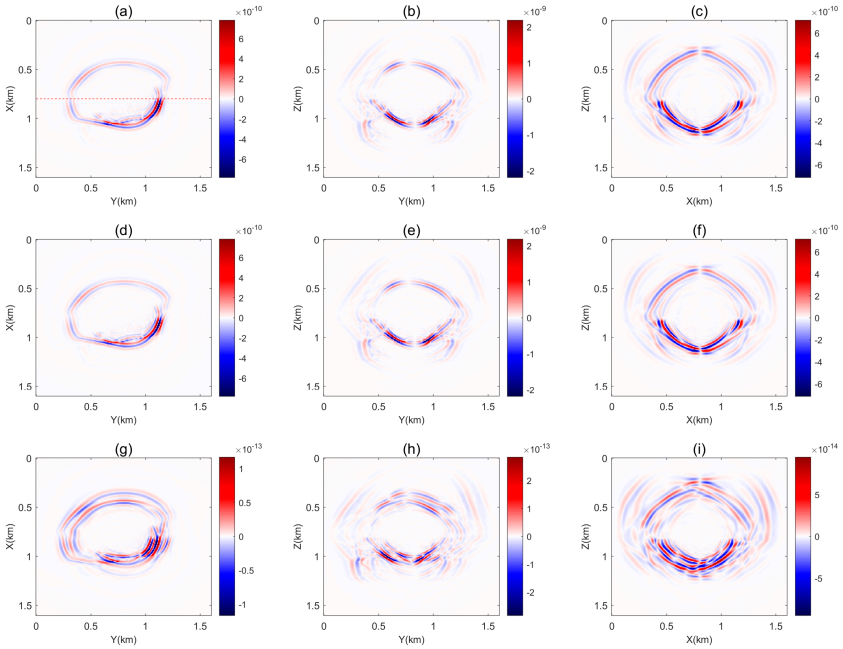


Figure 8. Orthogonal slices of 3D wavefields of the heterogeneous anisotropic model: (**a**–**c**) wavefields before sparsification; (**d**–**f**) wavefields after sparsification; (**g**–**i**) residual slices between wavefields before and after sparsification. The red dashed line in (**a**) indicates the slice position shown in Figure 9.

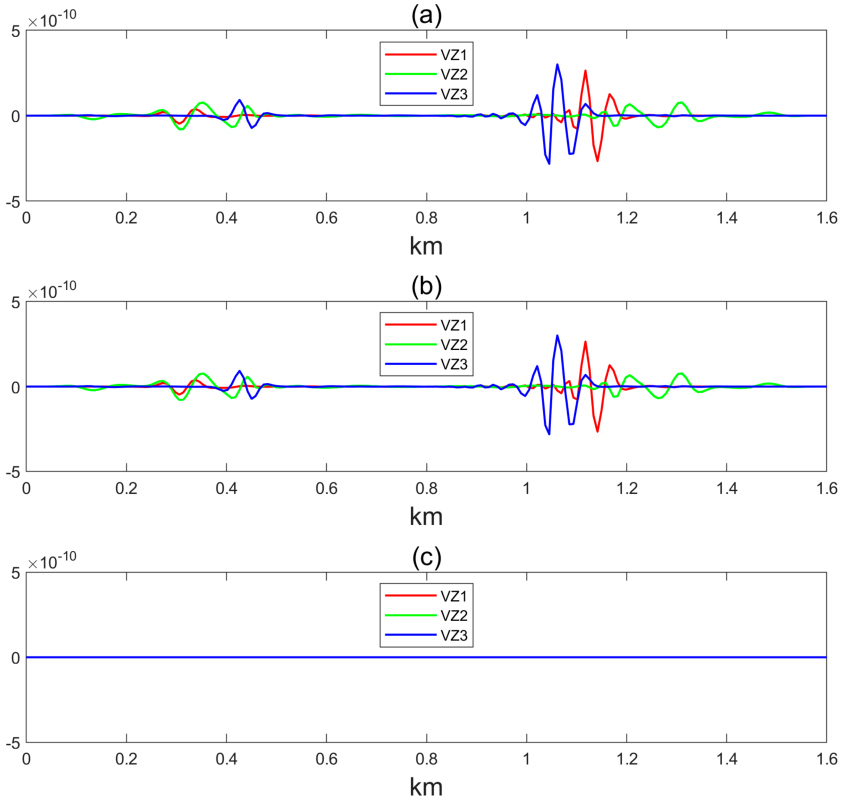


Figure 9. 1D wavefield curves of the heterogeneous anisotropic model: (**a**) wavefields before sparsification; (**b**) wavefields after sparsification; (**c**) residual curves between (**a**) and (**b**).

Figure 8 displays orthogonal slices of the three-dimensional wavefield for the heterogeneous anisotropic model, consisting of nine subgraphs arranged in three rows and three columns. Subplots (a)–(c) present orthogonal slices of the original 3D wavefield obtained without sparsification treatment. Subplots (d)–(f) illustrate the corresponding

orthogonal wavefield slices after the sparsification strategy is implemented. Subplots (g)–(i) show the residual slices calculated by subtracting the sparsified wavefield from the original wavefield, which quantitatively reflect the difference between wavefield results before and after sparsification.

As illustrated in Figure 8, the wavefield residuals are extremely small, with magnitudes 3–4 orders of magnitude lower than the original wavefield. This indicates that the sparsification algorithm barely affects the forward modeling accuracy for the homogeneous isotropic model. Figure 9 presents the one-dimensional wavefield profiles extracted along the slices shown in Figure 8. It can be further observed from Figure 9 that the two sets of wavefield data are highly consistent, and the relative error calculated from the residuals is only 0.021%.

Table 2 presents the statistical forward-modeling error metrics for the four aforementioned models before and after sparsification. It can be observed from the statistics that both the calculated absolute and relative errors are considerably small.

Table 2. Statistical Table of Three-Component Mean Computational Errors Before and After Sparsification.

Model	Homogeneous Isotropic Model	Homogeneous Anisotropic Model	Heterogeneous Isotropic Model	Heterogeneous Anisotropic Model
absolute error	2.42×10^{-4}	2.11×10^{-4}	2.13×10^{-4}	1.90×10^{-4}
relative error	0.023%	0.03%	0.021%	0.021%

Consistent phenomena can be observed across all four computational models. The wavefield discrepancies between sparsified and original results are trivial, with residuals about 3 to 4 orders of magnitude lower than the original wavefield and extremely small relative errors. The uniform performance over various models further proves that the sparsification method barely compromises calculation precision.

3.2. Computational Efficiency Comparison

To validate the speedup performance of the sparse matrix method proposed in this study, parallel forward modeling experiments were conducted on a system equipped with an Intel i9-7940HX CPU and an NVIDIA RTX 4070 GPU. Three models with different grid sizes ($100 \times 100 \times 100$, $150 \times 150 \times 150$, and $200 \times 200 \times 200$) were used for the simulations. The total number of time steps for the forward modeling was set to 200. Table 3 summarizes the computational time required for each model before and after applying the sparse matrix optimization.

Table 3. Table of Computational Time Statistics for Different Models Before and After Sparsification.

Model	$100 \times 100 \times 100$	$150 \times 150 \times 150$	$200 \times 200 \times 200$
before sparsification	1.9 s	11 s	39.6 s
after sparsification	1.1 s	5.1 s	12.9 s
speedup ratio	1.7	2.2	3.1

The results in Table 3 indicate clear differences in computational time before and after sparsification across different model scales. For the three model sizes ($100 \times 100 \times 100$, $150 \times 150 \times 150$, and $200 \times 200 \times 200$), the computation times before sparsification are 1.9 s, 11 s, and 39.6 s, respectively. After applying sparse matrix optimization, the corresponding times are reduced to 1.1 s, 5.1 s, and 12.9 s. The resulting speedup ratios are 1.7, 2.2, and 3.1. It can be observed that the acceleration effect becomes more pronounced as the model size

increases. In particular, for the largest model ($200 \times 200 \times 200$), the speedup reaches 3.1, demonstrating that the sparse matrix method effectively reduces computational cost and provides significantly greater performance benefits for large-scale forward modeling.

4. Discussion

The numerical experiments conducted in this study demonstrate that the proposed sparse-matrix acceleration strategy for the compact staggered finite-difference method achieves a favorable balance between computational efficiency and numerical accuracy. Across all four representative geological models—homogeneous isotropic, homogeneous anisotropic, heterogeneous isotropic, and heterogeneous anisotropic—the wavefield residuals between the original compact scheme and the sparsified implementation remain on the order of 10^{-3} to 10^{-4} relative to the original wavefield amplitudes. The relative errors, calculated as the ratio of residual energy to the original wavefield energy, are consistently below 0.03% in all cases. This small discrepancy confirms that sparsifying the derivative matrix by exponentially discarding decaying off-diagonal entries below a prescribed threshold introduces virtually no degradation in simulation accuracy. The preservation of high accuracy is particularly noteworthy in heterogeneous and anisotropic media, where wavefield complexity and directional variations are more pronounced, indicating that the sparse approximation effectively retains the essential coupling information required to accurately describe wave propagation.

From a computational perspective, the efficiency gains achieved by the proposed method are substantial and scale favorably with model size. For the three grid sizes tested (100^3, 150^3, and 200^3), the observed speedup ratios of $1.7\times$, $2.2\times$, and $3.1\times$, respectively, reveal a clear trend: the larger the model, the greater the acceleration. This behavior is expected because the dense matrix operations in the original compact finite-difference scheme scale quadratically with the number of grid points, whereas the sparse representation reduces both memory usage and floating-point operations to near-linear complexity. The exponential decay of the inverse matrix entries, as analyzed in Section 2.3, provides a basis for the band-limited or threshold-based truncation, and the results confirm that this truncation is highly effective for large-scale 3D problems where computational bottlenecks are most pronounced. Moreover, the combination of sparse storage with GPU-based parallel computing takes advantage of the memory bandwidth and thread-level parallelism of modern hardware, further improving the speedup for industrially relevant model sizes.

It is also worth noting that the proposed acceleration strategy does not compromise the inherent advantages of compact finite-difference methods, namely their low numerical dispersion and high phase accuracy. The wavefield snapshots and 1D profiles in Figures 2–9 show that the sparsified wavefields maintain the same waveform shapes, arrival times, and amplitude variations as the original solutions, with only negligible high-frequency noise introduced at the truncation boundaries. This robustness across different medium complexities highlights the generality of the approach, making it suitable for a wide range of seismic exploration scenarios, including full-waveform inversion and reverse-time migration, where both accuracy and computational cost are critical.

Compared with other acceleration techniques, such as conventional stencil optimization or purely data-driven machine learning surrogates, the proposed method retains the interpretability and deterministic nature of the underlying physics while providing a practical, hardware-aware implementation. It does not require extensive training data or hyperparameter tuning, and it can be readily integrated into existing finite-difference workflows. Future work may explore adaptive threshold selection based on local model properties, as well as hybrid schemes that combine sparsification with additional domain-decomposition strategies for even larger-scale simulations on distributed memory systems.

5. Conclusions

In this study, we have developed a high-precision and computationally efficient framework for the parallel numerical simulation of 3D anisotropic elastic wave equations, based on compact staggered finite-difference theory with sparse-matrix acceleration. The key contributions and findings are summarized as follows:

Accuracy preservation: Through comprehensive numerical experiments on homogeneous and heterogeneous, isotropic and anisotropic models, we have demonstrated that the sparsification of the derivative matrix—by retaining only the dominant near-diagonal entries—introduces negligible errors (relative errors $< 0.03\%$) while fully preserving the low-dispersion and high-accuracy characteristics of the original compact finite-difference scheme.

Computational efficiency: The proposed method achieves significant speedups that increase with model size, reaching up to $3.1\times$ for a 200^3 grid on a GPU-accelerated system. This improvement is attributed to the reduced memory requirements for memory access and efficient sparse matrix operations, effectively alleviating the computational bottleneck associated with dense matrix operations in 3D anisotropic elastic wave simulations.

Scalability and practicality: Equipped with sparse representation and GPU-accelerated computing, the proposed method enables efficient and accurate seismic forward modeling. The approach is deterministic, easy to implement, and compatible with existing high-performance computing infrastructures, offering a practical solution for high-resolution imaging and inversion in complex geological settings.

Broader implications: By enabling efficient and accurate wavefield simulation in anisotropic media, this work contributes to improved subsurface characterization, particularly in areas with dipping shale layers, fractured reservoirs, or folded sedimentary formations. The methodology can be extended to viscoelastic and poroelastic media, as well as to other PDE-based simulation tasks requiring high-order compact discretizations.

In conclusion, the sparse-matrix accelerated compact finite-difference method presented here effectively addresses the long-standing challenge of applying high-accuracy compact schemes to large-scale 3D anisotropic elastic wave simulation. Validated by GPU-based numerical tests on medium-scale models, the proposed method exhibits reliable accuracy and high computational efficiency. It offers a practical tool for seismic exploration and geological structure detection, with promising potential for further algorithmic optimization.

Author Contributions: Conceptualization, L.J. and Y.W.; Software, L.J. and C.Z.; Methodology, H.W. and C.Z.; Validation, Y.W. and C.Z.; Writing—Review and Editing, L.J. and H.W.; Funding Acquisition, L.J., H.W., M.W. and C.Z.; Project Administration, Y.W. All authors have read and agreed to the published version of the manuscript.

Funding: This research was funded by Open Fund of SINOPEC Key Laboratory of Enhanced Oil Recovery for Fractured Vuggy Reservoirs, grant number 34400000-25-ZC0607-0156.

Institutional Review Board Statement: Not applicable.

Informed Consent Statement: Not applicable.

Data Availability Statement: The original contributions presented in this study are included in the article. Further inquiries can be directed to the corresponding author.

Acknowledgments: The authors acknowledge the support from Open Fund of SINOPEC Key Laboratory of Enhanced Oil Recovery for Fractured Vuggy Reservoirs (grant no. 34400000-25-ZC0607-0156).

Conflicts of Interest: Author Lin Jiang, Huan Wen, Ming Wang, and Changjian Zhang were employed by the company Northwest Oilfield Company, SINOPEC. The remaining authors declare that the research was conducted in the absence of any commercial or financial relationships that could be construed as a potential conflict of interest.

References

1. Etgen, J.T.; O'Brien, M.J. Computational methods for large-scale 3D acoustic finite-difference modeling: A tutorial. *Geophysics* **2007**, *72*, SM223–SM230. [CrossRef]
2. Shragge, J.; Tapley, B. Solving the tensorial 3D acoustic wave equation: A mimetic finite-difference time-domain approach. *Geophysics* **2017**, *82*, T183–T196. [CrossRef]
3. Malovichko, M.; Khokhlov, N.; Yavich, N.; Zhdanov, M. Acoustic 3D modeling by the method of integral equations. *Comput. Geosci.* **2018**, *111*, 223–234. [CrossRef]
4. Lecoulant, J.; Guennou, C.; Guillon, L.; Royer, J.-Y. Three-dimensional modeling of earthquake generated acoustic waves in the ocean in simplified configurations. *J. Acoust. Soc. Am.* **2019**, *146*, 2113–2123. [CrossRef]
5. Vidana Morales, R.Y.; Ortega Cisneros, S.; Camacho Perez, J.R.; Sandoval Ibarra, F.; Casas Carrillo, R. 3D simulation-based acoustic wave resonator analysis using FEM. *Sensors* **2021**, *21*, 2715. [CrossRef]
6. Yang, H.; Fu, L.Y.; Li, H.; Du, Q.; Zheng, H. 3D acoustoelastic FD modeling of elastic wave propagation in prestressed solid media. *J. Geophys. Eng.* **2023**, *20*, 297–311. [CrossRef]
7. Zhang, T.; Trad, D.; Innanen, K. Learning to solve the elastic wave equation with Fourier neural operators. *Geophysics* **2023**, *88*, T101–T119. [CrossRef]
8. Lehmann, F.; Gatti, F.; Bertin, M.; Clouteau, D. 3D elastic wave propagation with a factorized Fourier neural operator (F-FNO). *Comput. Methods Appl. Mech. Eng.* **2024**, *420*, 116718. [CrossRef]
9. He, X.; Yang, D.; Huang, J.; Huang, X. Modeling 3-D elastic wave propagation in TI media using DG method. *IEEE Trans. Geosci. Remote Sens.* **2023**, *61*, 5904514. [CrossRef]
10. Zou, C.; Azizzadenesheli, K.; Ross, Z.E.; Clayton, R.W. Deep neural Helmholtz operators for 3-D elastic wave propagation. *Geophys. J. Int.* **2024**, *239*, 1469–1484. [CrossRef]
11. Nitka, M.; Rucka, M. 3D DEM modelling of acoustic emission in concrete. *Ultrasonics* **2025**, *150*, 107599. [CrossRef]
12. Li, C.; Zhao, H.; Hao, Y. A feature enhanced autoencoder integrated with Fourier neural operator for intelligent elastic wavefield modeling. *IEEE Trans. Geosci. Remote Sens.* **2025**, *63*, 5907016. [CrossRef]
13. Lyu, C.; Masson, Y.; Romanowicz, B.; Zhao, L. Distributional finite difference method for 3D seismic wave propagation. *JGR Solid Earth* **2024**, *129*, e2023JB027576. [CrossRef]
14. Han, B.; Xie, X.B. Wavefield reconstruction for elastic RTM. *Geophysics* **2023**, *88*, S87–S100. [CrossRef]
15. Zuo, J.; Niu, F.; Liu, L.; Da, S.; Zhang, H.; Yang, J.; Zhang, L.; Zhao, Y. 3D anisotropic wavefield separation in RTM. *Surv. Geophys.* **2022**, *43*, 673–701. [CrossRef]
16. Li, H.; He, C.; Gong, Q.; Zhou, S.; Li, X.; Zou, C. TLM-CFSPML for 3D dynamic responses of a layered transversely isotropic half-space. *Comput. Geotech.* **2024**, *168*, 106131. [CrossRef]
17. Xu, Y.; Liao, J.; Zhou, L.; Liu, H.; Zhang, Q.; Xie, J.; Wang, L. Staggered-grid schemes for 3D anisotropic media. *Chin. J. Geophys.* **2023**, *66*, 1164–1179.
18. Zheng, J.; Meng, L.; Sun, Y.; Peng, S. GPU acceleration for anisotropic wave equation. *Int. J. Min. Sci. Tech.* **2023**, *33*, 403–410. [CrossRef]
19. Cao, J.; Brossier, R.; Cabrera, E.; De la Puente, J.; Métivier, L.; Tarayoun, A. GPU accelerated computing towards a fast and scalable seismic wave modelling in SEISCOPE SEM46 code. In *Sixth EAGE High Performance Computing Workshop*; European Association of Geoscientists & Engineers: Bunnik, The Netherlands, 2022; Volume 2022, pp. 1–5.
20. Tan, J.Y.; Liu, G.F.; Gao, J.Y. GPU-based 3D seismic modeling. *CT Theory Appl.* **2022**, *25*, 1–12. [CrossRef]
21. Cai, W.; Zhu, P.; Li, Z. Multi-GPU CUDA-aware MPI seismic modeling. *Comput. Geosci.* **2024**, *190*, 105616.
22. Cao, W.; Li, Q.; Zhang, J.; Zhang, W. Accelerating 2D and 3D frequency-domain seismic wave modeling through interpolating frequency-domain wavefields by deep learning. *Geophysics* **2022**, *87*, T315–T328. [CrossRef]
23. Abdi, N.; Aminikhah, H.; Sheikhani, A.H.R. Compact finite difference for fractional models. *Chaos Solitons Fractals* **2022**, *162*, 112423. [CrossRef]
24. Chen, Z.; Wang, Y.; Gui, Z. A Mixed-Order Compact Generalized Finite Difference Method for Stable Seismic Wavefield Simulation. *Appl. Numer. Math.* **2026**, *223*, 181–195. [CrossRef]
25. Chen, L.; Huang, J.; Fu, L.Y.; Peng, W.; Song, C.; Han, J. A compact high-order finite-difference method with optimized coefficients for 2D acoustic wave equation. *Remote Sens.* **2023**, *15*, 604. [CrossRef]
26. Pan, K.; Wang, P.; Xu, Y.; Zhou, X. Combined compact finite difference schemes for 2-D acoustic wave propagation. *J. Appl. Math. Comput.* **2025**, *71*, 3009–3035. [CrossRef]

27. Zhou, C.; Wu, W.; Sun, P.; Yin, W.; Li, X. The combined compact difference scheme applied to shear-wave reverse-time migration. *Appl. Sci.* **2022**, *12*, 7047. [CrossRef]
28. Boersma, B.J. A 6th order staggered compact finite difference method for the incompressible Navier–Stokes and scalar transport equations. *J. Comput. Phys.* **2011**, *230*, 4940–4954. [CrossRef]
29. Gray, R.M. Toeplitz and circulant matrices: A review. *Found. Trends Commun. Inf. Theory* **2006**, *2*, 155–239. [CrossRef]

Disclaimer/Publisher's Note: The statements, opinions and data contained in all publications are solely those of the individual author(s) and contributor(s) and not of MDPI and/or the editor(s). MDPI and/or the editor(s) disclaim responsibility for any injury to people or property resulting from any ideas, methods, instructions or products referred to in the content.